

Revealing texture induced abnormal tensile deformation behavior in additively manufactured Haynes 282 using crystal plasticity simulations

Indrajit Nandi^{1,2}, Nabeel Ahmad^{1,2}, Nima Shamsaei^{1,2}, Shuai Shao^{1,2*}

¹ National Center for Additive Manufacturing Excellence (NCAME), Auburn University, Auburn, AL
36849, USA

² Department of Mechanical Engineering, Auburn University, Auburn, AL 36849, USA

*Corresponding author: sshao@auburn.edu
Phone: (334) 844-4839

Abstract

A ductile fracture typically features a dimpled surface appearance because of micro-void coalescence and a circular cup-and-cone morphology. Tensile fracture surfaces of additively manufactured Haynes 282, a nickel-base superalloy, in this work exhibit an elliptical shape – an aberration to classic fracture surface. Both microstructural characterization and fractography were performed using scanning electron microscopy (SEM) on the tensile deformed surfaces to assess the fracture behavior. To gain better mechanistic insights into the governing factors of this elliptical shape fracture, crystal plasticity finite element (CPFE) simulations were performed using the experimentally calibrated material parameters. Uniaxial tensile loading simulations were carried out on a polycrystalline aggregate where the initial texture was varied to the CPFE simulation to emulate the experimental microstructure. The mechanical response and shape of the fracture surface obtained from the simulations were compared with the experimental tensile deformed surface to illustrate the texture dependent deformation inhomogeneity.

Keywords: Additive manufacturing; Laser powder bed fusion; Crystal plasticity finite element simulation; Tensile fracture

Introduction

Haynes 282 alloy (UNS N07208) is a new γ' -precipitate-hardened nickel-based superalloy developed in 2005 by Haynes International [1]. Unique combination of creep strength, thermal stability, and good welding characteristics makes the alloy suitable for high temperature applications. Some recent studies have shown the suitability of processing Haynes 282 using the additive manufacturing (AM) technique [2]. AM has received significant attention from biomedical, aerospace, and automotive industries because of the capability to fabricate complex geometries and near-net-shaped components [3,4]. Given that Haynes 282 is a relatively new alloy, knowledge and understanding of mechanical, as well as fracture behaviors of additively manufactured (AMed) Haynes 282 specimens, are still limited.

It is well known that ductile fracture starts with void nucleation that forms at the inclusions, precipitates, second phases particles, etc., due to plastic deformation. These microvoids coalesce, grow and subsequently lead to fracture under the imposed strain [5]. Such fracture surfaces under tensile loading typically exhibit cup-and-cone morphology, having a well-defined central fibrous region and shear lip

regions [6]. Interestingly, tensile fracture surfaces from a recent study on laser powder bed fused (L-PBF) Haynes 282 [7] were shown to be elliptical under tensile loading. A similar fracture morphology was also observed by Murray et al. [8] on L-PBF CoCr. While these studies highlighted the unique morphology of fracture surfaces, a mechanistic understanding of this phenomenon was lacking. Understanding such fracture mechanisms will help improve the existing predictive ductile fracture models [9].

This study aims to examine the cause of elliptical-shaped tensile fracture of L-PBF Haynes 282 using integrated microstructural analysis and simulation approaches. Tensile loading on a polycrystalline aggregate has been modeled using CPFPE simulations to explain the experimental observation. Microstructural characterization and fractography analysis have been performed to understand the fracture behavior. Although this study investigates the fracture behavior of L-PBF Haynes 282, knowledge acquired from the CPFPE simulations will be beneficial for other ductile materials exhibiting similar fracture behavior.

Procedure and methodology

Experimental procedure

The specimens for this study were fabricated using L-PBF technology into near net-shaped parts. The feedstock powder particle was 15-45 μm in size. These specimens were heat-treated (HT) according to standard heat-treatment schedule [1,7], which is as following: solution annealing at 1135 $^{\circ}\text{C}$ for 1 hr followed by two-step aging at 1010 $^{\circ}\text{C}$ for 2 hr + 788 $^{\circ}\text{C}$ for 8 hr. Tensile testing was performed according to the ASTM-E8 standard [10] using a displacement rate of 0.012 mm/s. A Zeiss Crossbeam 550 scanning electron microscope (SEM) instrument equipped with an Oxford EBSD detector was used to analyze the microstructure and fractography. Microstructure samples were taken from an untested specimen and were cut in the transverse direction (TD), i.e., parallel to the build direction, and normal direction (ND), i.e., perpendicular to the build direction for the L-PBF specimens. The mounted specimens were then ground and polished with 320-2500 grit SiC sandpapers, followed by final polishing using ChemoMet with 0.05 μm colloidal silica suspension using an EcoMet TM30 semi-automatic grinder polisher. A final vibratory polishing step was carried out using a 0.02 μm colloidal silica suspension for 12 hours. Specimens were further cleansed thoroughly prior to performing EBSD analysis. MATLAB MTEX toolbox was used for postprocessing the EBSD results [11].

Computational Methodology

Three-dimensional crystal plasticity finite element simulations were performed using ABAQUS® through a user material subroutine (UMAT) [12]. The elasto-viscoplastic response of a metallic polycrystalline aggregate can be modeled using this UMAT with an explicit polycrystalline scheme. During the plastic deformation of the polycrystalline, only slip mechanisms were modeled, and twinning mechanisms were ignored due to the lack of twinning. A cylindrical polycrystalline aggregate consisting of 226 grains was adopted from Zhang et al. [12], which were generated and meshed using Neper, an open-source software package for polycrystal generation and meshing [13], using the Voronoi-based tessellation method as illustrated in Figure 1.

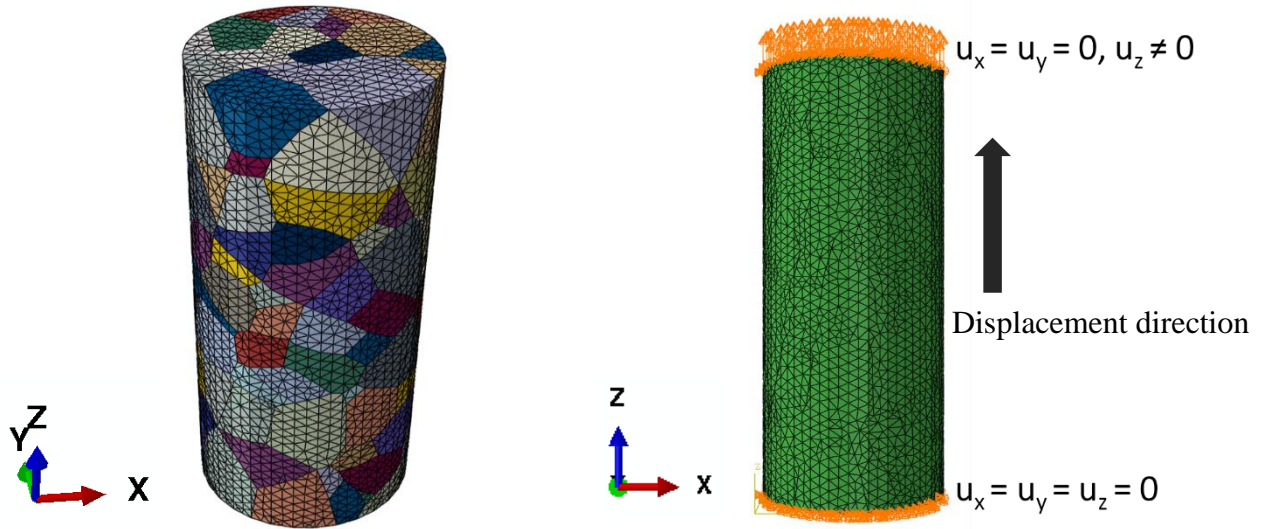


Figure 1. Illustration of the CPFE simulation set up; cylindrical shape polycrystalline aggregate of 226 grains with finite element meshes containing 110,295 elements along with the boundary conditions.

Symmetric boundary conditions were applied to the x- and y- directions without allowing any displacements in either of them ($u_x = u_y = 0$). The simulation geometry was allowed to deform along the [001] direction, i.e., the z-axis under the uniaxial tensile loading condition, as illustrated in Figure 1. The finite element mesh composed of 110295 elements were considered for the simulation. Identical geometry and meshing schemes were employed for all the simulations performed in this study. The elastic and plastic material constants were calibrated by capturing the stress-strain response of a “virtual single crystal” (VSC) simulations [14,15] and fitted to the experimental tensile test data reported in Figure 2. The VSC simulation was performed with a geometry comprising 500 grains using the mean-field assumptions. The calibrated elastic and plastic flow constants used for the Haynes 282 material are reported in Table 1. While the details of the crystal plasticity formulation followed in this study had been described in the work of Zhang et al.[12], key equations where the parameters presented in Table 1 are addressed here.

The following flow rule has been used to define the shear rate ($\dot{\gamma}_\alpha$) of the material:

$$\dot{\gamma}^\alpha = \dot{\gamma}_0 \left[\frac{|\tau_\alpha|}{\kappa_s^\alpha} \right]^{1/m} \text{sgn}(\tau^\alpha) \quad (1)$$

here $\dot{\gamma}^\alpha$ is the shear strain rate of slip system α , $\dot{\gamma}_0$ is the reference rate of the shear strain, τ_α is the resolved shear stress, κ_s^α is the critical resolved shear stress (CRSS) on slip system α , and m is the strain rate sensitivity. The CRSS can be defined as follows:

$$\kappa_s^\alpha = h_0 \left(\frac{\kappa_{s,s}^\alpha - \kappa_s^\alpha}{\kappa_{s,s}^\alpha - \kappa_{s,0}^\alpha} \right) \sum_{\alpha=1}^{12} |\dot{\gamma}_\alpha| \quad (2)$$

here, $\kappa_{s,0}^\alpha$ is the starting and $\kappa_{s,S}^\alpha$ is the saturation CRSS of slip system α , h_0 is the initial strain hardening rate, evolved due to dislocation accumulations. Here C_{11} , C_{12} , and C_{44} are components of the elastic stiffness matrix [15].

Table 1. Elastic and plastic material parameter constants used for the L-PBF Haynes 282.

C_{11} (GPa)	C_{12} (GPa)	C_{44} (GPa)	h_0 (MPa)	$\mathcal{K}_{s,0}^\alpha$ (MPa)	$\mathcal{K}_{s,S}^\alpha$ (MPa)	m	$\dot{\gamma}_0$
250.20	170.30	100.50	250	50	200	0.05	1.0

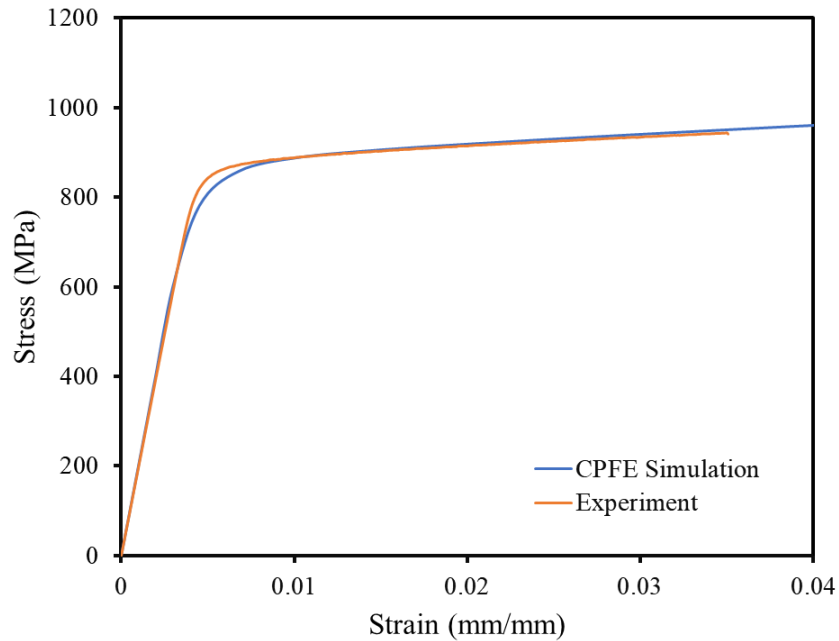


Figure 2. A comparison between experimental tensile response of Haynes 282 and VSC CPFE simulations comprising 500 grains using the mean-field assumptions.

Results and Discussions

Fractography analysis was performed on the fully HT tensile fracture surfaces, and the results are shown in Figure 3. It can be seen that the fracture surface comprises a central fibrous region, surrounded by a semi-conical region showing elliptical shape. The deformed shape deviates from the typical resemblance of a fracture surface and shows strong directionality upon axial loading. This was attributed to the initial textured microstructure of the L-PBF H282 specimens. Furthermore, microstructural analysis was performed on a large cross-sectional area extracted in both the (001) plane (ND) and (110) plane (TD) from a fully HT undeformed specimen.

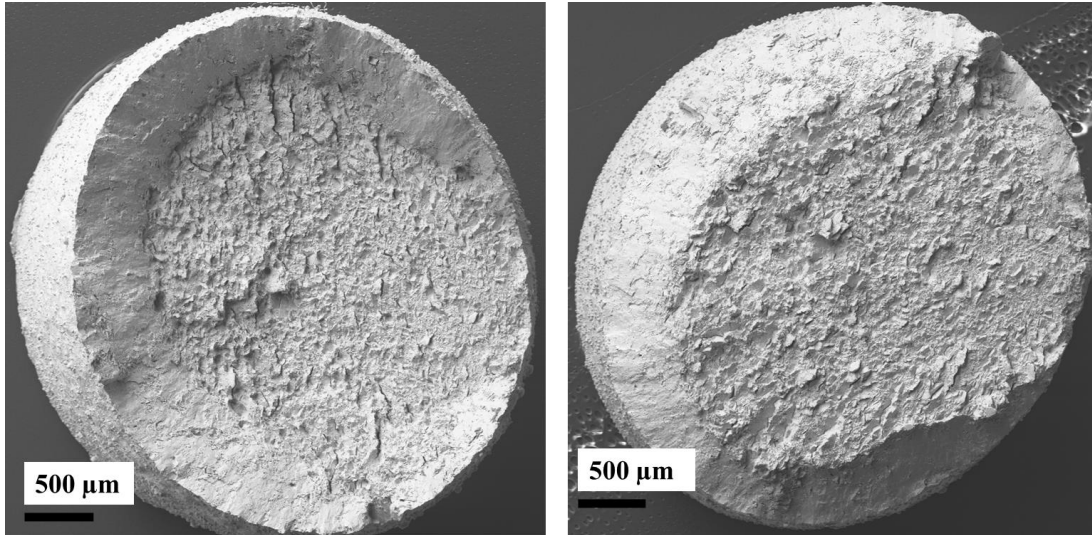


Figure 3. The fracture surfaces of both portions of the tested sample showing elliptical shape deformation.

Inverse pole figure (IPF) maps of both TD and ND are presented in Figure 4. It can be seen from the figure that the orientation of the grains is directional, and a certain texture is present in the material. Indeed, this was confirmed by the pole figure depicted in Figure 5(a), representative of the ND direction of the microstructure, showed directional behavior in the grain orientation and nearly close to being a single crystal.

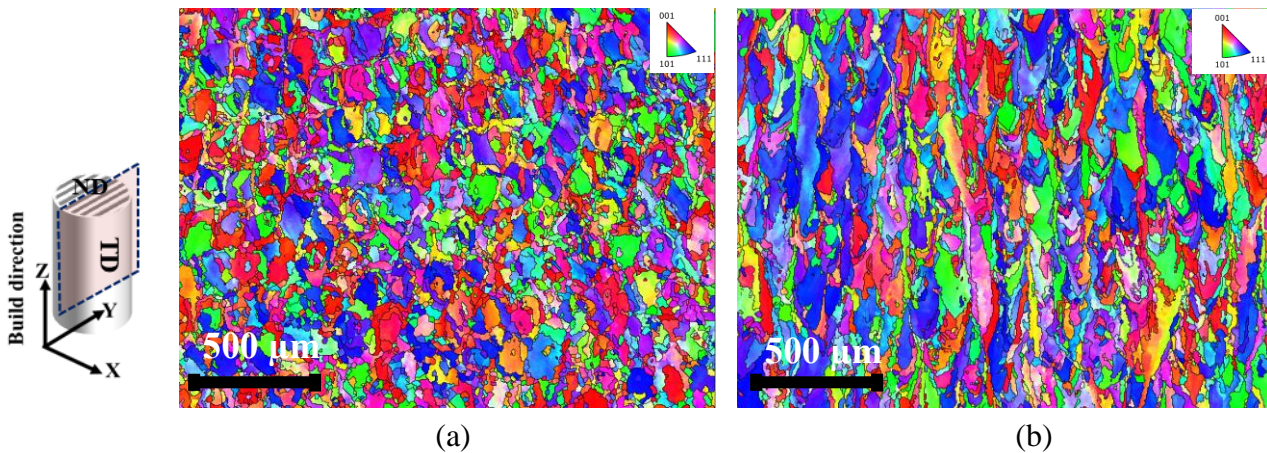


Figure 4. Orientation maps showing the grain morphology of the L-PBF Haynes 282 in; (a) normal direction (ND) and (b) transverse direction (TD). Microstructural samples were collected from untested HT specimens.

To further investigate the influence of texture in the fabricated samples, a virtual hypothetical orientation map has been created with axially symmetric crystallographic orientation relation, where the local crystal co-ordinates of each grain are directed along the specimen coordinate system. An ideal case satisfying this observation is shown in where each grain has the orientation: $[100]//x$, $[010]//y$, $[001]//z$ which would point to strong a single crystal texture. Due to the symmetry, the (100) pole figure with respect to the specimen co-ordinate system represents a strong (100) texture, as both coordinate systems are aligned in the same direction. Rotating the material points with by 45° respect to the z-axis and

followed by a similar rotation about the x-axis, i.e., the Euler angles following the bungee convention $(\phi_1, \Phi, \phi_2) = (45^\circ, 45^\circ, 0)$, also indicates a strong single crystal texture where the (100) pole figure with respect to the specimen co-ordinates are shown in Figure 5(c), which are similar to the pole figure obtained from the experimental analysis, therefore validating the textured microstructure of fabricated L-PBF Hayne 282 specimen.

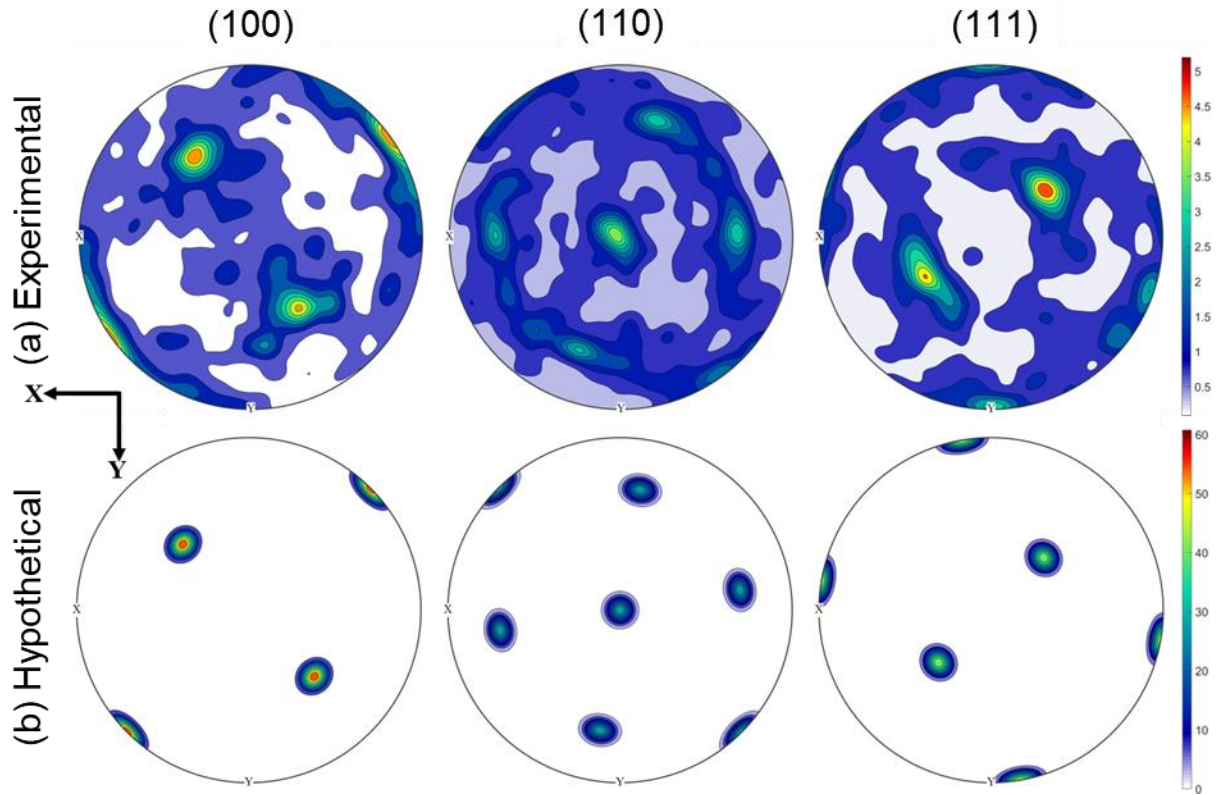


Figure 5. Representation of the pole figure obtained from: (a) an experimental microstructure along the ND, and (b) a hypothetical orientation map resembling the experimental texture.

To verify the influence of texture in the elliptical-shaped fracture surface observed during the tensile test, crystal plasticity finite element (CPFE) simulations of tensile deformation were performed in ABAQUS®. Detail description of the simulation geometry and meshing procedure was described in the methodology section. As seen in Figure 5(a & b), the pole figure obtained from the hypothetical orientation map emulates the one obtained from the experiment, and a parametric study of six tensile simulations was performed. The combinations of crystallographic orientations assigned to the individual geometry of each simulation are shown as a percentage in Table 2. Out of the 226 grains with random orientations, grains in a definite interval were assigned the same orientations, and all the grains were eventually composed of two distinct Euler angles. Due to a lack of misorientation angles between neighboring grains, the polycrystal acted like a single crystal when only one Euler angle was assigned to all the grains.

Table 2. Summary of all CPFE simulations of the polycrystalline aggregate performed in this study (individual models are indicated by their case number).

Monotonic Tensile Test: CPFE simulations						
Orientation	Simulation Cases					
(ϕ_1, Φ, ϕ_2)	(a)	(b)	(c)	(d)	(e)	(f)
$(0^\circ, 0^\circ, 0^\circ)$	100%	80%	60%	40%	20%	0%
$(45^\circ, 45^\circ, 0^\circ)$	0%	20%	40%	60%	80%	100%

Due to the anisotropic crystallography of the FCC crystal, the shape of the geometry changed after deformation. As it can be seen from Figure 6, when the crystal co-ordinates were directed along the specimen co-ordinate, i.e., Euler angles $(0^\circ, 0^\circ, 0^\circ)$, the deformed surface shows a circular shape under axial loading and resembles a single crystal behavior. As we start to introduce rotated crystallographic orientation to selected material points with particular Euler angles, i.e., $(45^\circ, 45^\circ, 0^\circ)$, the deformation shape starts elongating diagonally. When all the material points were assigned the same Euler angles, i.e., $(45^\circ, 45^\circ, 0^\circ)$, the deformation shows an elliptical shape phenomenon similar to the fracture surfaces observed in experimental tensile fracture surfaces L-PBF Haynes 282.

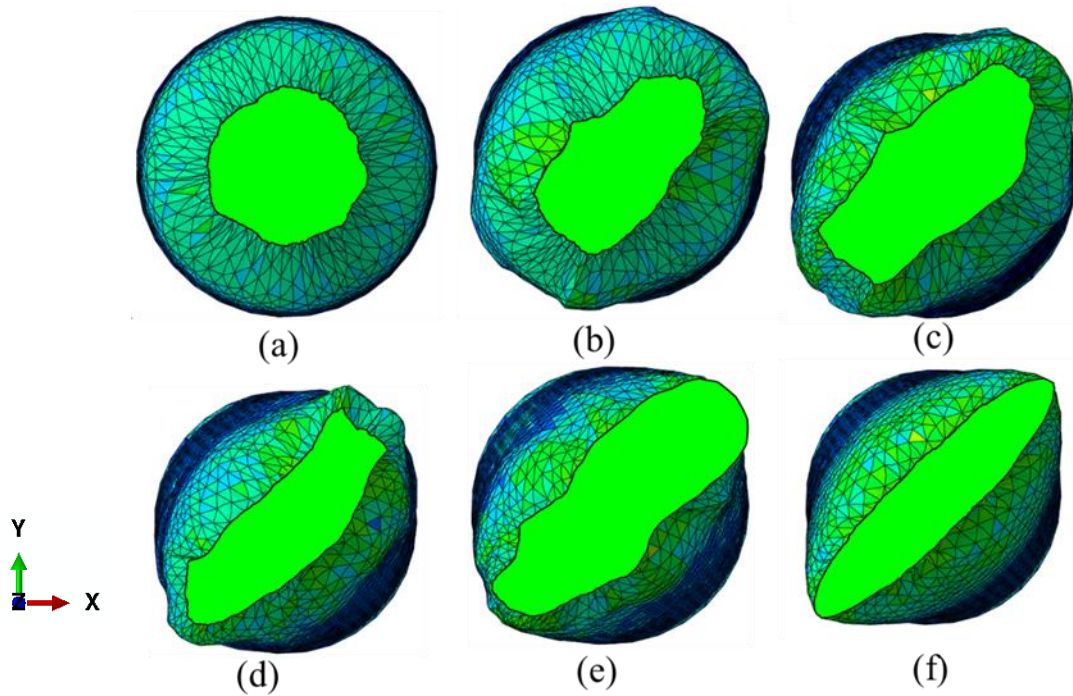


Figure 6. Cross-sectional view of the deformed geometry from (001) plane after tensile simulations showing the evolution of texture for the crystal orientations presented in Table 2, in ascending order, with the CPFE framework performed in ABAQUS.

Conclusion

This study used microstructural analysis and crystal plasticity finite element simulations to investigate the abnormal tensile deformation behavior observed in laser powder bed fused (L-PBF) Haynes 282. The following conclusions can be drawn from this study:

- The ductile fracture surface of the tensile specimen showed an elliptic shape rather than a typical cup-and-cone shape, ascribed to the presence of strong texture in the initial microstructure.
- Crystal plasticity finite element simulations further validated the texture dependency by showing the evolution of cross-sectional view of the simulation geometry from (001) direction, being circular to an ellipse, confirming the influence of initial texture on the abnormal elliptical shape deformation of a tensile tested L-PBF Haynes 282.

Acknowledgment

This paper is based upon the work partially funded by the National Aeronautics and Space Administration (NASA) under Award No. 80MSFC19C0010. This paper describes objective technical results and analysis. Any subjective views or opinions that might be expressed in the paper do not necessarily represent the views of the NASA or the United States Government.

References

- [1] International H. HAYNES ® 282 ® alloy. 2020.
- [2] Unocic KA, Kirka MM, Cakmak E, Greeley D, Okello AO, Dryepondt S. Evaluation of additive electron beam melting of haynes 282 alloy. *Mater Sci Eng A* 2020;772:138607. <https://doi.org/10.1016/j.msea.2019.138607>.
- [3] Lee S, Ahmad N, Corriveau K, Himel C, Silva DF, Shamsaei N. Bending properties of additively manufactured commercially pure titanium (CPTi) limited contact dynamic compression plate (LC-DCP) constructs: Effect of surface treatment. *J Mech Behav Biomed Mater* 2022;126:105042. <https://doi.org/10.1016/j.jmbbm.2021.105042>.
- [4] DebRoy T, Wei HL, Zuback JS, Mukherjee T, Elmer JW, Milewski JO, et al. Additive manufacturing of metallic components – Process, structure and properties. *Prog Mater Sci* 2018;92:112–224. <https://doi.org/10.1016/j.pmatsci.2017.10.001>.
- [5] Avateffazeli M, Carrion PE, Shachi-Amirkhiz B, Pirgazi H, Mohammadi M, Shamsaei N, et al. Correlation between tensile properties, microstructure, and processing routes of an Al–Cu–Mg–Ag–TiB₂ (A205) alloy: Additive manufacturing and casting. *Mater Sci Eng A* 2022;841:142989. <https://doi.org/10.1016/J.MSEA.2022.142989>.
- [6] Ghiaasiaan R, Muhammad M, Gradl PR, Shao S, Shamsaei N. Superior tensile properties of Hastelloy X enabled by additive manufacturing. *Mater Res Lett* 2021;9:308–14. <https://doi.org/10.1080/21663831.2021.1911870>.
- [7] Ghiaasiaan R, Ahmad N, Gradl PR, Shao S, Shamsaei N. Additively manufactured Haynes 282: effect of unimodal vs. bimodal γ' - microstructure on mechanical properties. *Mater Sci Eng A* 2022;831:142234. <https://doi.org/10.1016/j.msea.2021.142234>.

- [8] Murray SP, Pusch KM, Polonsky AT, Torbet CJ, Seward GGE, Zhou N, et al. A defect-resistant Co–Ni superalloy for 3D printing. *Nat Commun* 2020;11:1–11. <https://doi.org/10.1038/s41467-020-18775-0>.
- [9] Mu L, Zang Y, Wang Y, Li XL, Araujo Stemler PM. Phenomenological uncoupled ductile fracture model considering different void deformation modes for sheet metal forming. *Int J Mech Sci* 2018;141:408–23. <https://doi.org/10.1016/J.IJMECSCI.2018.04.025>.
- [10] Committee, E08 AE. Standard Test Methods for Tension Testing of Metallic Materials. ASTM International; 2020.
- [11] Niessen F, Nyyssönen T, Gazder AA, Hielscher R. Parent grain reconstruction from partially or fully transformed microstructures in $\{it\}$ MTEX}. *J Appl Crystallogr* 2022;55:180–94. <https://doi.org/10.1107/S1600576721011560>.
- [12] Zhang B, Dodaran M, Ahmed S, Shao S, Meng WJ, Juul KJ, et al. Grain-size affected mechanical response and deformation behavior in microscale reverse extrusion. *Materialia* 2019;6:100272. <https://doi.org/10.1016/j.mtla.2019.100272>.
- [13] Quey R, Dawson PR, Barbe F. Large-scale 3D random polycrystals for the finite element method: Generation, meshing and remeshing. *Comput Methods Appl Mech Eng* 2011;200:1729–45. <https://doi.org/10.1016/J.CMA.2011.01.002>.
- [14] Lienert U, Han TS, Almer J, Dawson PR, Leffers T, Margulies L, et al. Investigating the effect of grain interaction during plastic deformation of copper. *Acta Mater* 2004;52:4461–7. <https://doi.org/10.1016/j.actamat.2004.05.051>.
- [15] Marin EB. On the formulation of a crystal plasticity model. *Sandia Rep* 2006:4170.